Computer Methods and Programs in Biomedicine 165 (2018) 1–12

Contents lists available at ScienceDirect

Computer Methods and Programs in Biomedicine

journal homepage: www.elsevier.com/locate/cmpb

Computer-aided diagnosis of glaucoma using fundus images: A review

Yuki Hagiwara[a], Joel En Wei Koh[a], Jen Hong Tan[l], Sulatha V. Bhandary[b], Augustinus Laude[c,d], Edward J. Ciaccio[e], Louis Tong[f,g,h,i], U. Rajendra Acharya[a,j,k,*]

[a] Department of Electronics and Computer Engineering, Ngee Ann Polytechnic, 599489, Singapore
[b] Department of Ophthalmology, Kasturba Medical College, Manipal, India
[c] National Healthcare Group Eye Institute, Tan Tock Seng Hospital, Singapore
[d] Lee Kong Chian School of Medicine, Nanyang Technological University, Singapore
[e] Department of Medicine, Columbia University, New York, USA
[f] Ocular Surface Research Group, Singapore Eye Research Institute, Singapore
[g] Cornea and External Eye Disease Service, Singapore National Eye Center, Singapore
[h] Eye Academic Clinical Program, Duke-NUS Medical School, Singapore
[i] Department of Ophthalmology, Yong Loo Lin School of Medicine, National University of Singapore, Singapore
[j] Department of Biomedical Engineering, School of Science and Technology, Singapore School of Social Sciences, Singapore
[k] School of Medicine, Faculty of Health and Medical Sciences, Taylor's University, Subang Jaya, Malaysia
[l] National University of Singapore, Institute of System Science

ARTICLE INFO

Article history:
Received 20 April 2018
Revised 2 July 2018
Accepted 25 July 2018

Keywords:
Computer-aided detection system
Deep learning
Glaucoma
Machine learning
Optic disc
Segmentation

ABSTRACT

Background and objectives: Glaucoma is an eye condition which leads to permanent blindness when the disease progresses to an advanced stage. It occurs due to inappropriate intraocular pressure within the eye, resulting in damage to the optic nerve. Glaucoma does not exhibit any symptoms in its nascent stage and thus, it is important to diagnose early to prevent blindness. Fundus photography is widely used by ophthalmologists to assist in diagnosis of glaucoma and is cost-effective.
Methods: The morphological features of the disc that is characteristic of glaucoma are clearly seen in the fundus images. However, manual inspection of the acquired fundus images may be prone to inter-observer variation. Therefore, a computer-aided detection (CAD) system is proposed to make an accurate, reliable and fast diagnosis of glaucoma based on the optic nerve features of fundus imaging. In this paper, we reviewed existing techniques to automatically diagnose glaucoma.
Results: The use of CAD is very effective in the diagnosis of glaucoma and can assist the clinicians to alleviate their workload significantly. We have also discussed the advantages of employing state-of-art techniques, including deep learning (DL), when developing the automated system. The DL methods are effective in glaucoma diagnosis.
Conclusions: Novel DL algorithms with big data availability are required to develop a reliable CAD system. Such techniques can be employed to diagnose other eye diseases accurately.

1. Introduction

Glaucoma is a cluster of eye diseases that damage the optic nerve. The optic nerve is injured due to an elevated or inappropriate intraocular pressure (IOP) in the eye [101]. This is due to an imbalance between the amount of intraocular fluid produced in the eye and the amount of fluid that is drained. The fluid pressure builds up within the eye, when the eye is unable to drain away the excess fluid [38]. The pressure pushes against the optic nerve, damaging the nerve fibers. The injured nerve fibers cause the deterioration of the retinal nerve fiber layer (RNFL) and result in the enlarged cup-to-disc ratio (CDR) (or "cupping") and optic disc (OD) or optic nerve head (ONH) [81]. It can also induce thinning of the retina and retinal pigment epithelium around the optic nerve, known as peripapillary atrophy (PPA). Studies have shown that an increase in PPA can correspond to accelerating glaucoma [99]. Moreover, PPA can also be associated with high myopia [42]. Fig. 1 depicts the anatomy of a normal and a glaucomatous eye. It can be seen from the illustration that there is drainage blockage, which eventually leads to damage of the optic nerve. However, the blockage may not be in the Schlemm's canal. It could also be blocked in the trabecular meshwork [78]. In addition, Fig. 2 illustrates how CDR and OD can be altered in glaucoma. The OD in the

* Corresponding author at: Department of Electronics and Computer Engineering, Ngee Ann Polytechnic, 599489, Singapore.
E-mail address: aru@np.edu.sg (U.R. Acharya).

https://doi.org/10.1016/j.cmpb.2018.07.012
0169-2607/

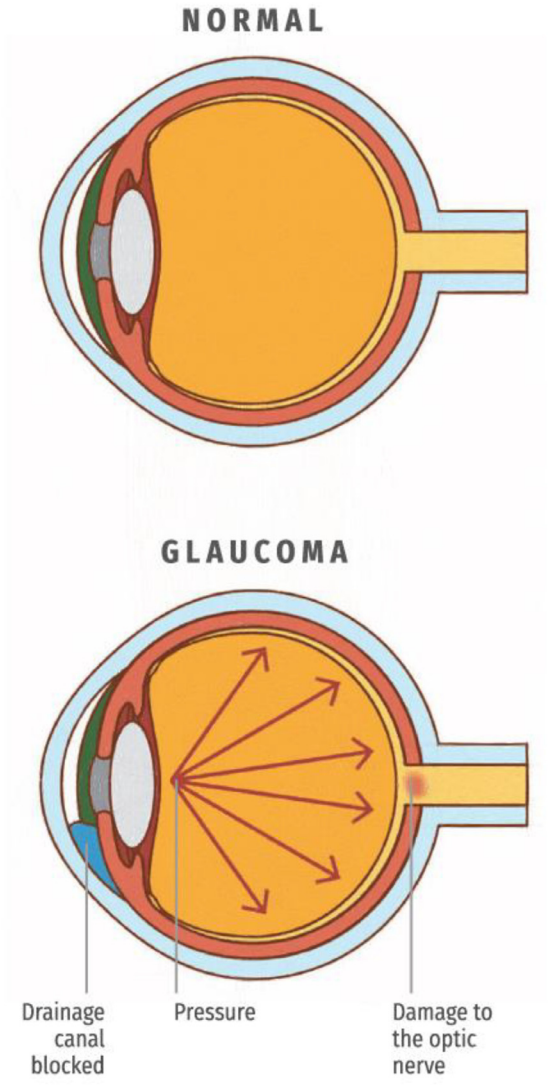

Fig. 1. The anatomy of a healthy and glaucoma tous eye.

glaucomatous image is enlarged as compared to the OD in normal fundus image.

Glaucomatous cupping can potentially be categorized into mild, moderate and severe classes, depending upon the values of the CDR. This is because any changes in the shape, width or breath of the OD are signs of possible glaucoma [11]. The CDR is determined by obtaining the ratio of the vertical diameter of the optic cup (OC) to the vertical diameter of the OD [24]. Fig. 3 shows examples of different stages of glaucomatous cupping.

(i) No glaucoma: The eye is graded with no glaucoma (normal) if the CDR is approximately 0.3.
(ii) Mild glaucomatous cupping: The eye is graded as mild glaucoma if the CDR is more than 0.4 but smaller than 0.5.
(iii) Moderate glaucomatous cupping: The eye is graded as moderate glaucoma if the CDR is between 0.5 and 0.8. In glaucoma, the loss of nerve fibers leads to loss of the neuroretinal rim, and exposure of the lamina cribrosa in the bottom of the cup.
(iv) Severe glaucomatous cupping: The eye is graded as having severe glaucoma if the CDR is greater than 0.8. However, there is a linear relationship between the disc size and cup. In a large disc above 2.2 mm, a CD of 0.8 is normal [11,24].

In addition, the classification of glaucoma (no, mild, moderate or severe) is also based upon the severity of the visual fields defects [72].

Glaucoma is often referred to as the "silent thief of sight" as it gradually and asymptomatically causes the loss of visual field [63]. The further degradation of the optic nerve can be prevented if it is diagnosed at an early stage. Hence, the American Academy of Ophthalmology encourages people aged between 40 and 64 years to attend regular eye screening once in 2–4 years and people over 65 years to screen for glaucoma once in every 1–2 years [35]. Glaucoma is the principal cause of irreversible blindness worldwide and it is predicted that the number of people diagnosed with glaucoma will rise from 76 million in 2020 to 111.8 million in 2040 [97]. Increased prevalence of this disease will increase the financial and social burden on economies, and the quality of life is reduced for glaucoma sufferers [101]. Hence, the early detection and treatment of glaucoma to prevent further damage can assist in addressing these problems.

2. Diagnostic approaches

Typically, ophthalmologists use perimetry to detect a defect in the visual field, pachymetry to measure the thickness of the cornea, tonometry to measure the IOP and ophthalmoscopy to diagnose glaucomatous cupping of the optic disc [98]. However, these clinical examinations are only conducted by the ophthalmologist when glaucoma is suspected [98].

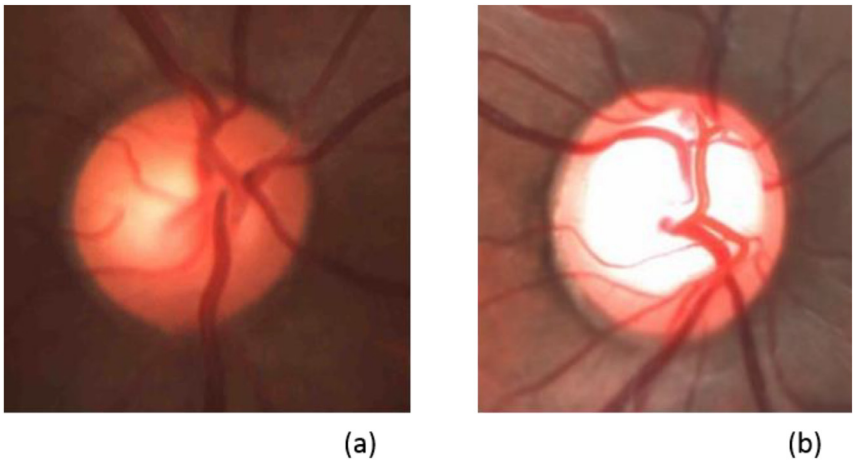

Fig. 2. An example of a zoomed-in (a) normal and (b) glaucomatous OD.

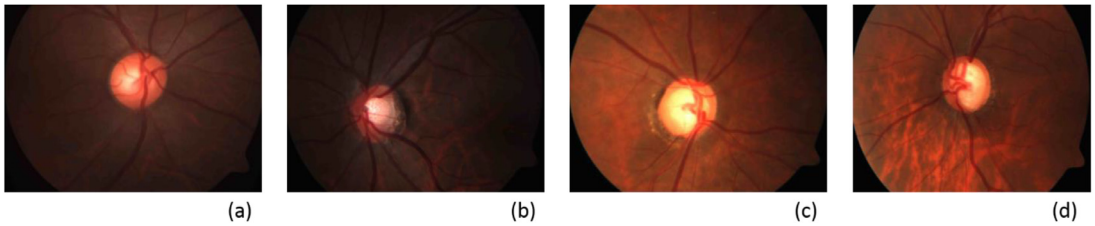

Fig. 3. Fundus images: (a) normal, (b) mild glaucoma, (c) moderate glaucoma and (d) severe glaucoma.

2.1. Retinal imaging technologies

The confocal scanning laser ophthalmoscopy (CSLO) [102], optical coherence tomography (OCT) [43] and scanning laser polarimetry (SLP) [26,87] are the imaging modalities employed to detect the nerve fiber loss and optic disc changes in glaucoma, in addition to the clinical examinations [16,57,89].

(1) The CSLO uses a low-intensity laser with confocal microscopy to produce a tomogram of the optic nerve and retina [102]. The most common commercially available CSLO device is the Heidelberg retina tomograph (HRT) (by Heidelberg Engineering, Heidelberg, Germany). It enables imaging over relatively larger retinal areas and can be used to obtain 3-dimensional images. But, it is operator-dependent (via setting of the contour line and reference plane) and hence, may introduce inter-observer variabilities.
(2) The OCT is a noninvasive cross-sectional tool that utilizes low-coherence interferometry to construct a representation of the retina through optical scattering [43]. It provides for a fast data acquisition rate and quick diagnosis. However, it is costly and has limited penetration power.
(3) The SLP measures the thickness of RNFL with retinal laser ellipsometry [26]. The commercially available product of the SLP is the GDx (by Carl Zeiss Meditec, Dublin, California). The SLP is user-friendly and acquires images rapidly. However, it provides only RNFL data.

Overall, these retinal imaging instruments are bulky and costly. Furthermore, the retinal images obtained by these diagnostic tools require subjective evaluation by qualified experts, and it is time-consuming to manually inspect the individual retinal images [86,90]. In addition to these modalities, retinal images can also be obtained using a fundus camera, which is more economical and portable [1]. Moreover, the fundus images acquired from the fundus camera can facilitate the early detection of glaucoma in settings where more expensive equipment is not available [81]. Moreover, the fundus camera can also be used to identify other ocular conditions such as age-related macular degeneration (AMD) and diabetic retinopathy (DR). The AMD and DR are the other leading causes of blindness besides glaucoma [6,50–52]. Therefore, the fundus camera is a preferred mode of screening. Therefore, a single fundus image can be used to detect AMD, DR, glaucoma, maculopathy and normal classes. Hence, there is a need to develop an automated glaucoma diagnosis system which is reliable and fast. The remaining sections of this review paper cover the use of computer-aided detection (CAD) systems to accurately detect glaucoma. Section 3 focuses on the development of a CAD system, and the glaucoma risk index (GRI) is discussed in Section 4. State-of-the-art machine learning algorithms are described in Section 5, and the paper concludes in the last section (Section 6).

3. Computer-aided detection (CAD) system

The CAD system comprises of traditional machine learning techniques that follow a fixed procedure – (i) input image, (ii) pre-processing, (iii) segmentation, (iv) feature extraction, (v) feature selection or ranking and (vi) classification to construct the CAD system [92]. Fig. 4 shows the workflow of a general CAD system.

(i) *Input fundus image:* In addition to reviewing published works, we have also taken 30 normal and 30 glaucomatous fundus images from the Kasturba Medical College, Manipal, India to study the algorithms employed by these studies. These images were obtained using an FF450 ZEISS fundus camera with a resolution of 2588×1958 pixels, and were stored in JPEG format.
(ii) *Pre-processing*: Images obtained will be subjected to a pre-processing technique to enhance and standardize the input images prior to performing feature extraction. Contrast limited adaptive histogram equalization (CLAHE) [80] is commonly employed to improve the quality of the fundus images. Moreover, it reduces noise and artifact present in the fundus images. The CLAHE technique is applied to the 60 fundus images.
(iii) *Segmentation:* The segmentation of the region-of-interest (ROI) from the fundus images will be performed prior to feature extraction. The segmentation of the ROI process involves localizing the OD and then extracting features from the segmented OD [96]. In many recent studies, the diagnosis of glaucomatous optic discs is done without segmentation [2,8,59,60,74].

Table 1 summarizes selected studies used to segment OD. The active contour model (ACM) (snake model) [46,66,104], Attanassov intuitionistic fuzzy histon (A-IFSH)-based technique [67], clustering [21], polar transformation [65], superpixel classification [21], Otsu threshold [31], vascular bundle displacement [31] and watershed transformation [85] methods have been used in various studies to segment the OD. The detection of PPA and RNFL is assistive in the automated detection of glaucoma. Gabor filtering [40,70], textural analysis [69,75] and polar transform [76] are used to detect and evaluate the thickness of RNFL and PPA (see Table 2).

(i) *Features extraction:* Significant and distinctive features from the fundus images will be extracted during this process. The wavelet decomposition [27,59,68,91], image descriptor [81], morphological [45,48,71], non-linear [3,8,53,59,60,68,74], textural [2,3] and transformation [8,14,68,74,83] methods are applied on the fundus images to capture the concealed pixel variations in the images. The following feature extraction methods are employed in the studies in Table 3.

The discrete wavelet transform (DWT) [61], empirical wavelet transform (EWT) [34] and variational mode decomposition (VMD) [25] are used during feature extraction. Both DWT and EWT utilize low and high pass filters to decompose the images into coefficients. Then, these coefficients are subjected to further analysis. The VMD decomposes the images into different amplitude- and frequency-modulated coefficients. These transformation techniques decompose the images to obtain coefficients that are useful in differentiating the two classes of optic discs (normal and glaucoma). On the other hand, the GIST descriptor [77] which is a form of image descriptor that describes the visual features of the fundus images based upon various orientations and scales of the images, is also used for glaucoma detection. The morphological features such

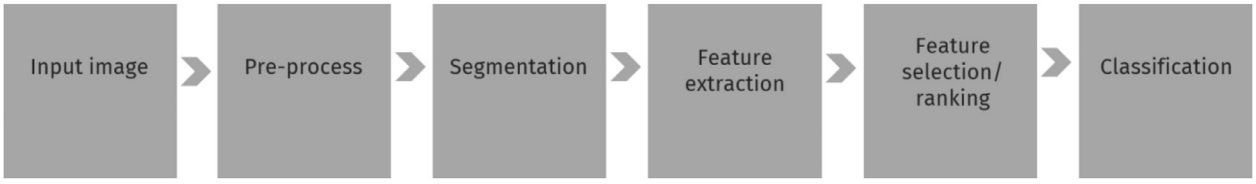

Fig. 4. The block diagram of a conventional CAD system.

Table 1
Selected studies on the segmentation of OD using fundus images.

Authors (Year)	Number of images (N: normal, G: glaucoma, DR: diabetic retinopathy)	Segmentation methodology	Performances
Merickel et al. (2007) [65]	**G**: 82	Polar transformation, region-based cost function	**Accuracy**: 93.89%
Joshi et al. (2011) [46]	**N**: 33, **G**: 105	ACM, vessel bend detection	**F-score**: 0.940
Xu et al. (2013) [104]	**Dataset 1:** **N**: 482, **G**: 168 **Dataset 2:** **N**: 1,630, **G**: 46	ACM, reconstruction-based technique	**Dataset 2:** **Area Under Curve**: 0.86 **Sensitivity**: 73.90% **Specificity**: 85.00%
Mookiah et al. (2013) [67]	**N**: 30, **G**: 39, **DR**: 31	A-IFSH	**Accuracy**: 93.40% **F-score**: 0.92 **Precision**: 0.93 **Recall**: 0.91
Cheng et al. (2013) [21]	**Dataset 1:** 650 **Dataset 2:** 1,676	Clustering algorithm, superpixel classification	**Dataset 1:** **Area under curve**: 0.800 **Dataset 2:** **Area under curve**: 0.822
Rajaiah et al. (2014) [85]	**G**: 50	LDA, optic disc area calculation, watershed transformation	**Accuracy**: 96.00%
de la Fuente-Arriaga (2014) [31]	**N**: 24, **G**: 43	Vascular bundle displacement, Otsu threshold	**Accuracy**: 91.34% **Sensitivity**: 93.02% **Specificity**: 91.66%
Mittapalli et al. (2016) [66]	**N**: 17, **G**: 42	ACM	**F-score**: 0.975

Table 2
Selected studies on the localization and detection of PPA or RNFL using fundus images.

Authors (Year)	Number of images (N: normal, G: glaucoma)	Methodology	Performances
Hayashi et al. (2007) [40]	**N**: 26, **G**: 26	• Removal of the blood vessel • Transformation into a rectangular array • Gabor filtering	**Accuracy**: 71%
Muramatsu et al. (2010) [70]	**N**: 81, **G**: 81	• Removal of the blood vessel • Gabor filtering	**Sensitivity**: 91%
Muramatsu et al. (2011) [69]	**N**: 88, **G**: 83	• Textural analysis • ACM	**Sensitivity**: 73% **Specificity**: 95%
Odstrcilik et al. (2014) [75]	**N**: 16, **G**: 8	• Textural analysis	–
Oh et al. (2015) [76]	**N**: 100, **G**: 98	• Blood vessel segmentation • Polar transform • Hough transform	**Sensitivity**: 86% **Specificity**: 75%

as CDR, the shift in the ONH, neuroretinal rim area, and blood vessels, are extracted to provide further information concerning the optic nerve head in the images.

The non-linear feature methods such as the entropy [88], fractal dimension (FD) [62] and higher-order spectra (HOS) [73] are extensively used to detect distinctive and subtle pixel variations in the images. The entropy feature is able to portray subtle variations in the fundus images. Hence it can be used to differentiate the two classes by analyzing the changes in the pixels of normal and glaucomatous images. The FD is typically employed to measure the non-uniformity in the pixels. The HOS method comprises of third and higher order cumulants and moments, that are useful in analyzing non-linear characteristics of the fundus images [3,68,74].

Furthermore, texton [47], local configuration pattern (LCP) [37], gray level co-occurrence matrix (GLCM) [39] and run-length matrix [33] are texture feature extraction methods employed to distinguish glaucomatous from normal fundus images. Texton is applied to the fundus images to produce an explicit pixel-based textural feature to characterize the two classes, using filters such as Schmid, Leung–Malik and maximum response. The images are convolved with these filters to produce different textons that illustrate the different textural characteristics of images. The LCP is a technique based upon the local binary pattern (LBP) texture descriptor. The LBP descriptor is analyzed by comparing the center pixel with circular neighboring pixels. The GLCM and run-length matrix are textural methods that measure the frequency of occurrence of a particular intensity of pixels in the fundus images. Numerical texture features can be derived from these methods.

Finally, the Gabor transform [32], modified census transformation (MCT) [30] and radon transform (RT) [82] typically convert the input fundus images into different frequency domains. These transformed features are used for classification. The Gabor transform technique requires the convolution of a Gabor kernel with the fundus image in order to depict the textural details at various orientations and frequencies of the images [8]. The MCT is an extension of the census transform, which compares the intensity pixel values of the center pixel with its neighboring pixels. Thus, the MCT can capture the different pixel variations in the images. The RT method is used to transform two-dimensional images into one-dimensional data by projecting the images along a radial line at different angles (from 0° to 170°). Therefore, distinct patterns of normal and glaucomatous images can be obtained at different an-

Table 3
Published studies on the CAD system to automatically diagnose glaucoma using fundus images.

Authors (Year)	Number of images	Methodology	Performances in %		
			Accuracy	Sensitivity	Specificity
Kolar et al. (2008) [53]	**N:** 14, **G**: 16	**Features**: FD **Classifier**: SVM (RBF, 0.5)	93.80	–	–
Nayak et al. (2009) [71]	**N**: 24, **G**: 37	**Features**: morphological **Classifier**: ANN (3-layers)	90.00	100.00	80.00
Bock et al. (2010) [14]	**N**: 336, **G**: 239	**Features**: PCA Glaucoma risk index	80.00	73.00	85.00
Acharya et al. (2011) [3]	**N**: 30, **G**: 30	**Features**: HOS, textural **Classifier**: SVM (RBF)	91.00	–	–
Dua et al. (2012) [27]	**N**: 30, **G**: 30	**Features**: DWT **Feature ranking**: chi-square, gain ratio, info gain, reliefF **Classifier**: SMO	93.33	–	–
Mookiah et al. (2012) [68]	**N**: 30, **G**: 30	**Features**: DWT, HOS, RT **Classifier**: SVM (Polynomial 2) Glaucoma risk index	93.33	86.67	93.33
Noronha et al. (2014) [74]	**N**: 100, **Mild G**: 72, **G**: 102	**Features**: HOS, RT **Feature reduction**: LDA **Classifier**: NB	92.65	100.00	92.00
Acharya et al. (2015) [8]	**N**: 266, **G**: 244	**Features**: Gabor transform, entropy **Feature reduction**: PCA **Feature ranking**: Bhattacharyya, ROC curve, *t*-test, Wilcoxon **Classifier**: SVM (Polynomial 1)	93.10	89.75	96.20
Issac et al. (2015) [45]	**N**: 35, **G**: 32	**Segmentation**: adaptive threshold **Features**: morphological features **Classifier**: SVM (RBF)	94.11	100.00	90.00
Singh et al. (2016) [91]	**N**: 30, **G**: 33	**Segmentation**: brightest pixel intensity **Features**: DWT **Feature reduction/selection**: PCA, GA **Classifier**: SVM (RBF)	94.75	100.00	90.91
Maheshwari et al. (2017) [59]	**N**: 30, **G**: 30	**Features**: EWT, correntropy **Classifier**: LS-SVM (RBF)	96.67	100.00	93.33
Maheshwari et al. (2017) [60]	**N**: 244, **G**: 244	**Features**: VMD, entropy, FD **Feature selection**: reliefF **Classifier**: LS-SVM (RBF)	94.79	93.62	95.88
Acharya et al. (2017) [2]	**N**: 143, **G**: 559	**Features**: texton, LCP **Feature ranking**: SFFS, *t*-test **Classifier**: KNN ($K=2$) Glaucoma risk index	95.70	96.20	93.70
Raghavendra et al. (2017) [83]	**N**: 500, **G**: 500	**Segmentation**: median filter **Features**: RT, MCT, GIST **Feature reduction**: LSDA **Classifier**: SVM (Polynomial 2)	97.00	97.80	95.80
Kausu et al. (2018) [48]	**N**: 51, **G**: 35	**Segmentation**: fuzzy c-means clustering, Otsu's thresholding **Features**: morphological, wavelet **Classifier**: MLP (ANN) (3 layers)	97.67	98.00	97.10

gles for classification. Principal component analysis (PCA) [79] is a data reduction approach that transforms the fundus images into a new orthogonal feature space, while retaining the information of the fundus images.

(i) *Feature selection or ranking:* the features extracted will be subjected to selection [2,91], reduction [8,71,81,91] or ranking [2,8,27,59] techniques to hand-pick the highly significant features that will be useful in the discrimination of normal versus glaucomatous class. If the number of extracted features is too many, then feature reduction techniques including principal component analysis [79], linear discriminant analysis [93], independent component analysis [44], locality sensitive discriminant analysis [15] and marginal fisher analysis [105] may be used to reduce the number of features for classification. The ranked features will be fed to the classifiers one by one depending upon their rank from the highest rank in descending order, until the maximum performance is achieved. Various ranking methods, namely Bhattacharya [13], entropy [88], receiver operating characteristics (ROC) [29], *t*-value [94] and Wilcoxon [103] can be used.

(ii) *Classification:* Finally, these selected or ranked features are fed into the classifier for the identification of normal versus glaucomatous class. Usually, the ten-fold cross-validation [28] technique is adopted to train the proposed CAD system. The efficacy of the proposed system is determined by the averaged accuracy, sensitivity and specificity. It can be noted from Table 3 that the support vector machine (SVM) [3,8,45,53,68,83,91] classifier is commonly employed in the CAD system to distinguish glaucomatous and normal fundus images. The SVM classifier is suitable for both linearly separable and linearly non-separable data. If the extracted features are linearly differentiable, a linear SVM classifier is employed. However, if the extracted features are non-linear, then kernel functions, namely the polynomial functions 1, 2 and 3 and the radial basis function, are implemented [100]. A few other classifiers, namely the artificial neural network (ANN) [48,71], K-nearest neighbor (KNN) [2], least square-support vector machine (LS-SVM) [59,60], naïve Bayes (NB) [74] and sequential minimal optimization (SMO) [27] are implemented to automatically differentiate the two classes based upon the input features. The ANN is a supervised classifier that has an input, a hidden layer that comprises of a huge number of interconnected neurons, and an output layer [106]. The KNN classifier is an instance-based classifier, where a test data is categorized into its respective class depending on the majority vote from k-nearest neighbors, where the value k is a variable [23]. NB is also a supervised technique that uses the Bayes

Table 4
Highly significant features in descending order with p-values < 0.05.

	Features	Normal		Glaucoma		
		Mean	SD	Mean	SD	t-value
C_{lda}^{11}	11_Cumulants_LDA1	0.14	0.09	0.77	0.10	24.81
C_{lda}^{14}	14_Cumulants_LDA1	0.12	0.08	0.75	0.12	24.11
L_{37}^{111}	37_LCP310_111	0.77	0.15	0.25	0.17	12.81
L_{40}^{100}	40_LCP310_100	0.77	0.14	0.28	0.16	12.58
G_{csa}	Sum average	0.79	0.11	0.43	0.20	8.62
$G_{rlrlglre}$	Long run low gray-level run emphasis	0.61	0.20	0.21	0.16	8.56
B_{amp}^{10}	HOS mAmp_10	0.56	0.20	0.16	0.15	8.55
$E_{rbio3.3}^{v}$	V3_Energy	0.62	0.23	0.22	0.13	8.39
$E_{rbio3.7}^{v}$	V5_Energy	0.59	0.23	0.20	0.12	8.23
B_{amp}^{1}	HOS mAmp_1	0.43	0.19	0.12	0.12	7.43
FD	Fractal dimension	0.81	0.13	0.55	0.15	7.15
V_{renyi}^{3}	VMD3_Renyi entropy	0.85	0.06	0.61	0.19	6.61
V_{kapoor}^{3}	VMD3_Kapoor entropy	0.65	0.14	0.36	0.21	6.40
Ga_{phVar}^{12}	Phase12_var	0.36	0.09	0.62	0.22	5.88
Ga_{phEne}^{11}	Phase11_energy	0.34	0.11	0.60	0.23	5.59
F_{pca}^{2}	FFT_PCA2	0.62	0.20	0.40	0.23	4.03
P_{pca}^{2}	PixelIntensity_PCA2	0.62	0.20	0.40	0.23	4.03
P_{pca}^{1}	PixelIntensity_PCA1	0.39	0.20	0.55	0.25	2.64
F_{pca}^{1}	FFT_PCA1	0.39	0.20	0.55	0.25	2.64
M_{lsda}^{13}	Radon-MCT-GIST_LSDA13	0.45	0.17	0.37	0.08	2.32
M_{lsda}^{1}	Radon-MCT-GIST_LSDA1	0.35	0.14	0.28	0.11	2.11

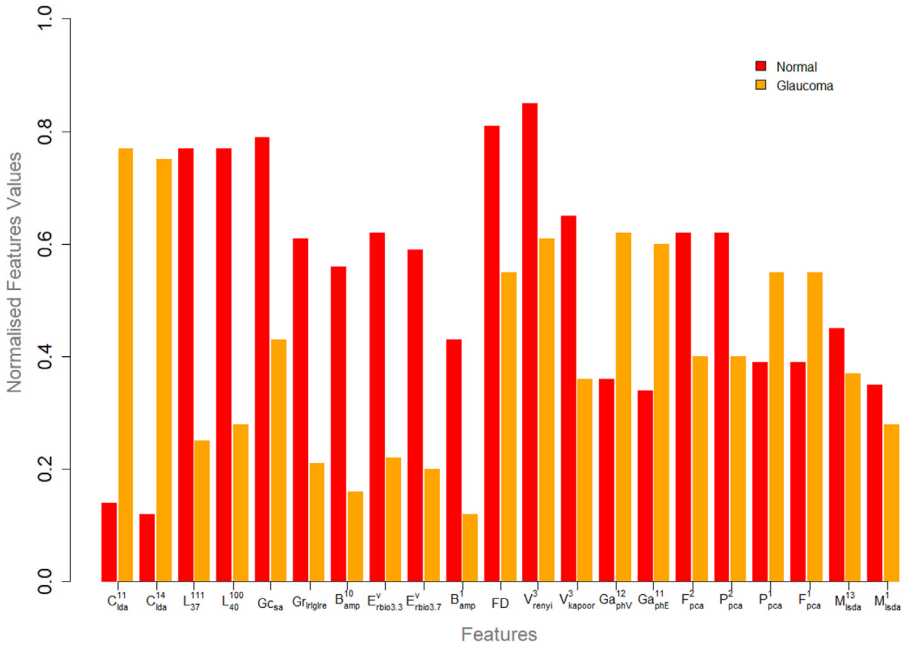

Fig. 5. Bar plot of ranked features based on Table 4.

theorem for classification. It classifies the test data by predicting the probability of the outcome, based upon the given conditions through the training of the data [28]. Lastly, the SMO is an enhanced algorithm to train the SVM classifier [49].

Table 3 records the published papers that implemented CAD in the automated diagnosis of glaucoma using fundus images, with groundtruth provided by the clinicians. The investigators employed different machine learning approaches in the construction of the CAD system. In this study, we have employed feature extraction techniques documented in Table 3. Then, the extracted features are subjected to the t-test [94], and were ranked according to their statistical significance.

The highly distinctive features extracted from the 60 fundus images with the normalized mean and standard deviation (SD) values are tabulated in Table 4. A visual illustration of the highly ranked features can also be seen in Fig. 5. Cumulants are the most statistically significant, with a t-value of 24.81 and the least statistically significant feature is the Radon-MCT-GIST feature with a t-value of 2.11. Fig. 6 portrays the cumulant plots for a sample of normal and glaucomatous fundus image. The eighteen plots in (a) and (b) each represent the HOS cumulant plots for every 10° from 0° to 170° The cumulant plots for the two classes are distinguishable, and therefore the features extracted from these plots can be used for the differentiation of normal and glaucomatous classes. The VMD decomposed components for a normal and glaucomatous image are represented in Fig. 7. The first image from the left represents the first mode of decomposition, with the rightmost representing the fifth level of decomposition. It can be noted that the decomposed coefficients are unique, and with the increase in the decomposition level more detailed information can be seen. Fig. 8 shows the spatial envelope energy spectrum of normal and glaucomatous fundus images obtained using the GIST technique. These

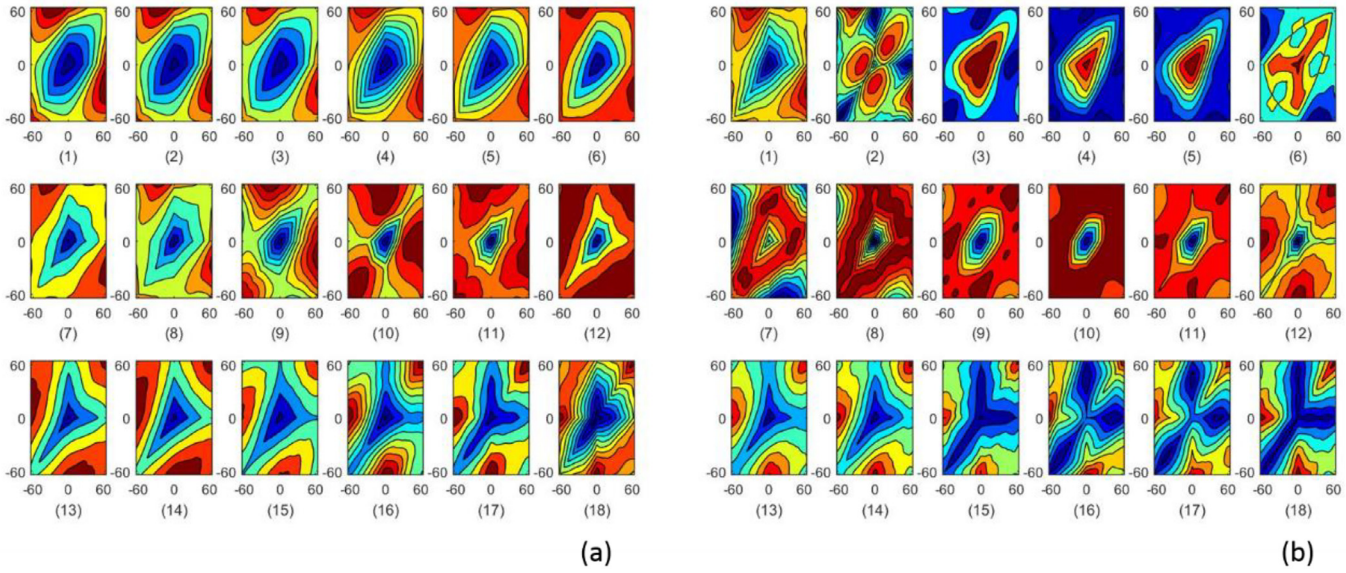

Fig. 6. Cumulant plots of (a) normal and (b) glaucomatous fundus images.

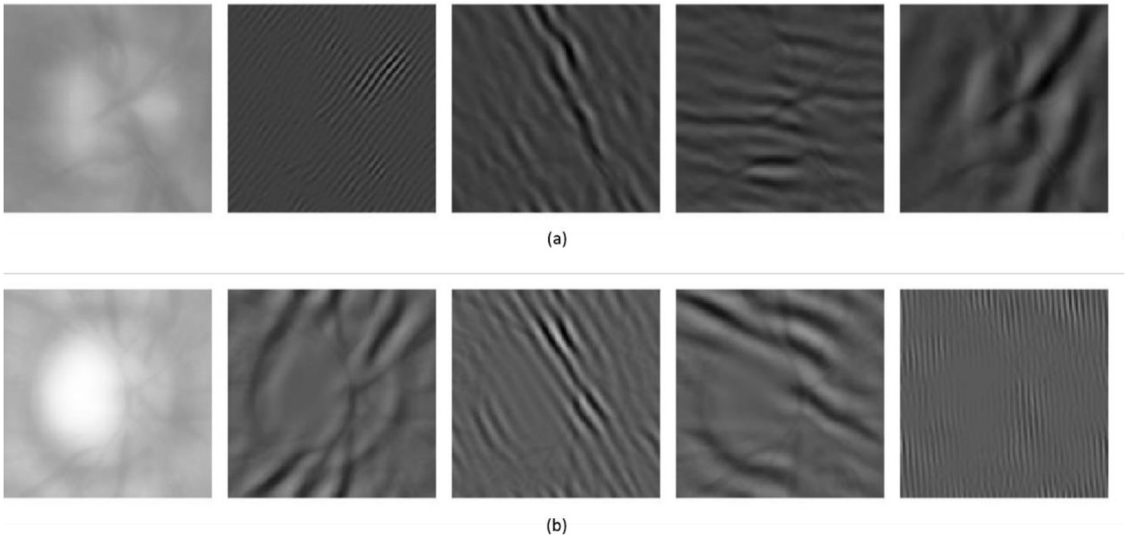

Fig. 7. VMD decomposed components of (a) normal and (b) glaucomatous fundus images.

GIST spectrums can be used to discriminate between the two classes.

4. Glaucoma risk index (GRI)

A risk index is derived from a mathematical equation that quantifies the two classes (normal and glaucomatous) using a single number. In the past, this concept has been employed by various researchers to discriminate between the two classes using medical images [4–7,9,10,95].

In this work, we have employed a similar technique and developed a glaucoma risk index (GRI) to distinguish glaucomatous images from normal. The most highly significant two features (from Table 4) are used to develop the GRI shown in Eq. (1). The two cumulant features are experimentally combined in the equation to obtain the maximum separation between the two classes (see Fig. 9). Our GRI can discriminate between the two classes clearly without any overlap. In the past, Acharya et al. [2], Bock et al. [14] and Mookiah et al. [68] have also developed a GRI to characterize normal and glaucoma classes (see Table 3) using different sets of features. However, the present GRI employed here is not from a single generalized equation. The equation used varies with the type of features extracted (i.e. entropy features, cumulant features) from the fundus images. Therefore, further empirical studies with large datasets are required to achieve a universal GRI.

$$GRI = (1.2 \times C_{lda}^{11}) + \left(8.1 \times C_{lda}^{14}\right) \quad (1)$$

5. Discussion

Currently, the deep learning (DL) technique, which is a branch of machine learning, is applied as a biomedical engineering technique to improve quality of life [56]. Researchers are turning away from the conventional CAD system to DL-based CAD systems. This is because DL networks have the ability to self-learn during the training of the network and hence, there is no need to have a hand-devised set of features for classification. Consequently, this

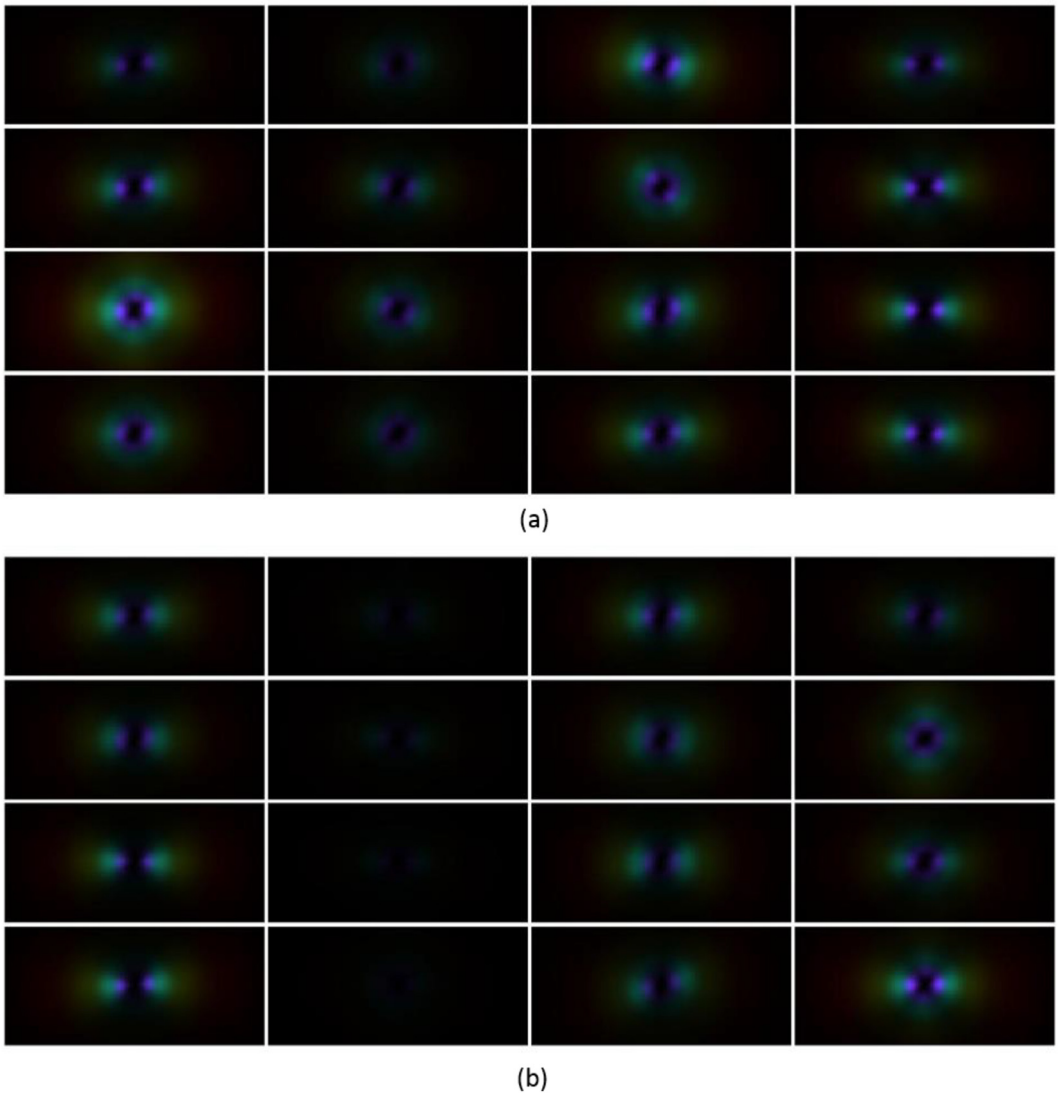

Fig. 8. Spatial envelope energy plots of (a) normal and (b) glaucomatous fundus images.

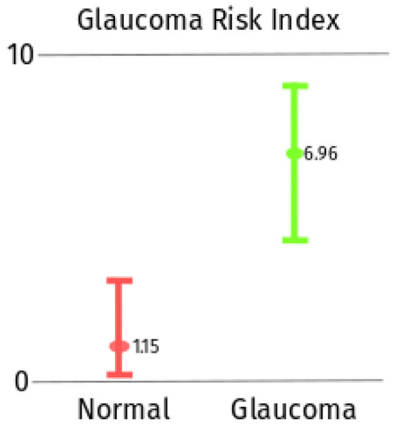

Fig. 9. Box plot of proposed GRI.

will also save significant engineering effort and time. The convolutional neural network (CNN) is the most widely implemented form of DL. It has been successfully employed in diverse fields, such as in the assessment of structural damage [58], handwriting recognition [22], and image recognition [54], including the assessment of medical images [54]. In general, a CNN model consists of (i) convolutional, (ii) pooling and (iii) fully-connected layers [55] (Fig. 10). The convolutional layer is mainly used to extract and learn features during training. The main function of pooling is to reduce the spatial dimension of the sample and at the same time, retain significant information. Lastly, the fully-connected layer denotes that every neuron in the previous layer is fully connected to the neurons in the current layer of the CNN model. The total number of output neurons signifies the number of classification classes.

Furthermore, autoencoder [12] and the long short-term memory (LSTM) [41] are different variations of DL that are commonly used in pattern recognition and handwriting recognition. An autoencoder is an unsupervised neural network that acquires significant information from the input data without guidance. Basically, an autoencoder consists of an encoder and decoder. It takes unlabeled input samples, encodes, and then reconstructs the output (decode). On the other hand, the LSTM is a recurrent network that has a memory block with three gate units, namely the input, forget, and output. Also, it has a built-in memory where it retains information based upon the previous computation.

A few researchers have experimented with DL methodology to develop an algorithm for an automated detection of the various eye diseases such as AMD, DR and glaucoma [36,99]. Chen et al.

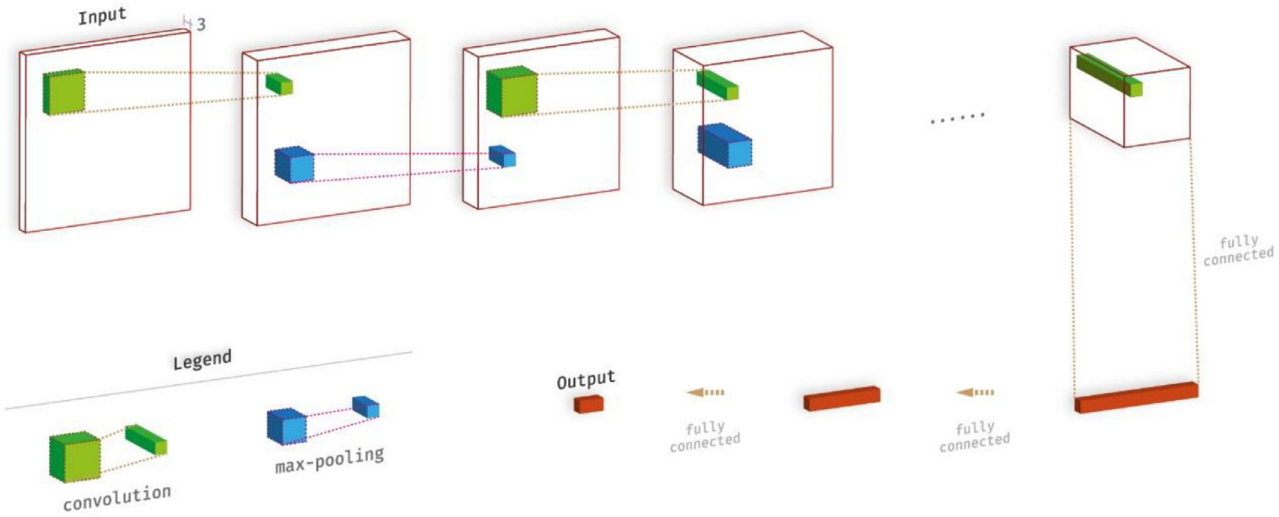

Fig. 10. An overview of a CNN architecture.

[19] developed a six-layer CNN model to distinguish glaucomatous fundus images from normal fundus images. In their study, they have experimented with their proposed network structure with two databases (dataset 1 and dataset 2) and obtained high area under curve (AUC) values of 0.831 and 0.887 respectively. The team has also modified their model to enhance the output performance of the classification with an AUC of 0.838 (dataset 1) and 0.898 (dataset 2) [20], when comparing their automated diagnosis scores versus clinician diagnosis.

Orlando et al. [77] adopted two different CNN architectures from OverFeat [85] and VGG-S [18], respectively, to develop a CNN model for automated detection of glaucoma. The main aim of utilizing pre-trained architectures from non-fundus images is to validate the existing CNN architectures (VGG-S and OverFeat) in the detection of glaucoma using the fundus images. The fundus images obtained are first pre-processed to enhance the quality of the images, and subsequently the segmentation of ONH is performed. The proposed architectures yielded AUC values of 0.763 and 0.718, respectively, with OverFeat and VGG-S. Groundtruth for these images was provided by four glaucoma experts. Chai et al. [17] initiated a two-fold CNN application to improve the overall identification of glaucoma. They applied the entire image to the CNN model and then the segmented optic disc region was fed as input to the CNN model. Thereafter concatenation of the CNN models was followed by a fully-connected layer for the classification. Their developed model attained a classification accuracy of 81.69%.

Instead of feeding the entire fundus image into the CNN model for classification, Zilly et al. [108] measured the CDR from the fundus images and evaluated the images according to the CDR values obtained. Their team employed CNN with entropy sampling, to localize and segment the ROI. They achieved an accuracy of 94.10% using CDR values. Raghavendra et al. [84] proposed an eighteen-layer CNN model using 1,426 fundus images (589 normal and 837 glaucomatous). Their network achieved a high sensitivity and specificity of 98.00% and 98.30%, respectively.

Hence, it can be concluded that DL-based CAD systems can improve diagnostic performance and make automated diagnostic systems more robust. The disadvantage of DL is that it needs a large database to train the DL model. The diagnostic efficiency of DL will be at its optimum with greater number of training images selected from the total number of images. This DL technique can be employed in healthcare applications to obtain accurate and high performance [63].

It can be noted from Fig. 5 and Table 4 that the cumulant features (nonlinear features) are highly distinctive. The cumulant plots at different angles for the normal fundus image appear to be more uniform as compared to the glaucomatous class due to the enlarged OD. It can be observed that there are distinct changes in the patterns of two classes at different angles (see Fig. 6(b)). This is because the HOS cumulants are able to capture the subtle pixel variations in the images. Similarly, the VMD and spatial envelope energy spectrum plots are unique for the two classes. The features extracted from these plots can be used for the classification of two classes.

It can be understood from Table 3 that high diagnostic performances are obtained in most of the studies. An example is the study by Kausu et al. [48]. They yielded the best diagnostic performance of 97.67%. Their group segmented the ROI first prior to the extraction of features. Also, they have used a mixture of morphological and wavelet features to determine the dominant features from the images. Most of the studies listed in Table 3 have obtained high accuracies in the characterization of glaucoma. This shows the ability of a CAD system to aid ophthalmologists in the screening of glaucoma. The CAD system is more efficient as compared to manual analysis as it is not subjective, and it is more reliable [107].

Nonetheless, the diagnostic performance of the CAD system can be further enhanced with DL. As mentioned in Section 5, DL is presently the most accurate and robust machine learning technique. It performs very well with big data, as it can capture the diverse range of features from the training dataset.

Currently, all of these existing works address the detection of glaucomatous fundus images. However, in a real setting, patients may have other eye diseases such as DR, AMD and cataracts, in addition to glaucoma. In the future, we intend to develop a system which can detect glaucoma even in the presence of other eye diseases. The DL may yield high classification performance even in the presence of the other diseases and when only low-resolution images are available.

It can be seen from the Table 5 that most of the authors have used their own private datasets to develop CAD systems. There is only one small public database [64]. Hence, to develop a robust accurate CAD system, it is important to have a large public database. This will be assistive in identifying the best-performing CAD system, as all the systems could use the same database.

Table 5
Published studies on different architectures of CNN models to automatically diagnose glaucoma using fundus images.

Authors (Year)	Number of images	Methodology	Performances Area under curve	Accuracy (%)	Sensitivity (%)	Specificity (%)
Chen et al. (2015) [19]	**(ORIGA dataset)** **Normal**: 482 **Glaucoma**: 168 **(SCES dataset)** **Normal**: 1630 **Glaucoma**:46	6-layer CNN	**ORIGA**: 0.831 **SCES**: 0.887	–	–	–
Chen et al. (2015) [20]	**(ORIGA dataset)** **Normal**: 482 **Glaucoma**: 168 **(SCES dataset)** **Normal**: 1630 **Glaucoma**: 46	6-layer CNN	**ORIGA**: 0.838 **SCES**: 0.898	–	–	–
Orlando et al. (2017) [77]	**(DRISHTI-GS1 dataset)** **Normal & Glaucoma**: 101	8-layer CNN (OverFeat and VGG-S architectures)	**OverFeat**: 0.763 **VGG-S**: 0.718	–	–	–
Chai et al. (2017) [17]	**(Beijing Tongren Hospital, China)** **Various Eye Diseases**: 2163 **Glaucoma**: 1391	Two-branch CNN	–	81.69	–	–
Zilly et al. (2017) [108]	**(DRISHTI-GS1 dataset)** **Normal**: 85 **Glaucoma**: 70	Hough transform, CNN, entropy sampling	–	94.10	92.30	95.60
Raghavendra et al. (2018) [84]	**(Kasturba Medical College, Manipal, India)** **Normal**: 589 **Glaucoma**: 837	18-layer CNN	–	98.13	98.00	98.30

SCES: Singapore Chinese Eye Study
DRISHTI-GS1: Aravind eye hospital, Madurai
*ORIGA: Online Retinal Fundus Image Database for Glaucoma Analysis and Research

6. Conclusion

Herein, the usefulness of CAD systems to impartially diagnose patients with glaucoma is discussed. Also, different machine learning techniques employed by researchers over the past decade are summarized. Based on the extraction of the different features employed in Table 3, it is observed that nonlinear features, especially cumulant features, could be useful to discriminate the subtle pixular difference between normal and glaucomatous fundus images relatively well. It is also been noted that DL has advantages over the conventional machine learning techniques, whereby very little hand-crafted features extraction and selection are needed. Additionally, any healthcare practitioners can take advantage of the CAD system to assist in screening for glaucoma. This will be especially helpful in geographical areas where ophthalmologists are scarce. Furthermore, the CAD system can also be implemented in the detection of glaucoma when other eye conditions need to be screened for.

Acknowledgment

The authors would like to express their sincere gratitude to the staffs from the Ophthalmology Department of Kasturba Medical College, Manipal, India for providing the normal and glaucomatous fundus images for this review paper.

Supplementary materials

Supplementary material associated with this article can be found, in the online version, at doi:10.1016/j.cmpb.2018.07.012.

References

[1] M.D. Abramoff, M.K. Garvin, M. Sonka, Retinal imaging and image analysis, IEEE Rev. Biomed. Eng. 3 (2010) 169–208.
[2] U.R. Acharya, S. Bhat, J.E.W. Koh, S.V. Bhandary, H. Adeli, A novel algorithm to detect glaucoma risk using texton and local configuration pattern features extracted from fundus images, Comput. Biol. Med. 88 (2017) 72–83.
[3] U.R. Acharya, S. Dua, X. Du, V.S. Sree, K.C. Chua, Automated diagnosis of glaucoma using texture and higher order spectra features, IEEE Trans. Inform. Technol. Biomed. 15 (3) (2011) 449–455.
[4] U.R. Acharya, H. Fujita, V.K. Sudarshan, M.R.K. Mookiah, J.E.W. Koh, J.H. Tan, Y. Hagiwara, K.C. Chua, S.P. Junnarkar, A. Vijayananthan, K.H. Ng, An integrated index for identification of fatty liver disease using radon transform and discrete cosine transform features in ultrasound images, Inf. Fus. 31 (2016) 43–53.
[5] U.R. Acharya, M.R.K. Mookiah, J.E.W. Koh, J.H. Tan, S.V. Bhandary, A.K. Rao, H. Fujita, Y. Hagiwara, K.C. Chua, A. Laude, Automated screening system for retinal health using bi-dimensional empirical mode decomposition and integrated index, Comput. Biol. Med. 75 (2016) 54–62.
[6] U.R. Acharya, M.R.K. Mookiah, J.E.W. Koh, J.H. Tan, K. Noronha, S.V. Bhandary, A.K. Rao, Y. Hagiwara, K.C. Chua, A. Laude, Novel risk index for the identification of age-related macular degeneration using radon transform and DWT features, Comput. Biol. Med. 73 (2016) 131–140.
[7] U.R. Acharya, M.R.K. Mookiah, J.E.W. Koh, J.H. Tan, K. Noronha, S.V. Bhandary, A.K. Rao, Y. Hagiwara, K.C. Chua, A. Laude, Automated diabetic macular edema (DME) grading system using DWT, DCT features and maculopathy index, Comput. Biol. Med. 84 (2017) 59–68.
[8] U.R. Acharya, E.Y.K. Ng, W.J.E. Lim, K.P. Noronha, C.M. Lim, K.P. Nayak, S.V. Bhandary, Decision support system for the glaucoma using Gabor transformation, Biomed. Signal Process. Control 15 (2015) 18–26.
[9] U.R. Acharya, E.Y.K. Ng, J.H. Tan, S.V. Sree, K.H. Ng, An integrated index for the identification of diabetic retinopathy stages using texture parameters, J. Med. Syst. 36 (2012) 2011–2020.
[10] U.R. Acharya, U. Raghavendra, H. Fujita, Y. Hagiwara, J.E.W. Koh, J.H. Tan, V.K. Sudarshan, A. Vijayananthan, C.H. Yeong, A. Gudigar, K.H. Ng, Automated characterization of fatty liver disease and cirrhosis using curvelet transform and entropy features extracted from ultrasound images, Comput. Biol. Med. 79 (2016) 250–258.
[11] A. Almazroa, R. Burman, K. Raahemifar, V. Laksminarayanan, Optic disc and optic cup segmentation methodologies for glaucoma image detection: a survey, J. Ophthalmol. 2015 (2015) 180972 28 pages.
[12] Y. Bengio, Learning deep architecture for AI, Found. Trends Mach. Learn. 2 (1) (2009) 1–127.
[13] A. Bhattacharyya, On a measure of divergence between two statistical populations defined by their probability distribution, Bull. Calcutta Math. Soc. 35 (1943) 99–109.

[14] R. Bock, J. Meier, L.G. Nyul, J. Hornegger, G. Michelson, Glaucoma risk index: automated glaucoma detection from color fundus images, Med. Image Anal. 14 (2010) 471–481.
[15] D. Cai, X. He, K. Zhou, J.I. Han, H. Bao, Locality sensitive discriminant analysis, in: Proceedings of the Twentieth International Joint Conference on Artificial Intelligence, 2007, pp. 708–713.
[16] L. Camejo, R.J. Noecker, Optic nerve imaging, in: Becker-Shaffer's diagnosis and therapy of the glaucomas E-book Part 3: Clinical Examination of the Eye, 2009, pp. 171–187.
[17] Y. Chai, L. He, Q. Mei, H. Liu, L. Xu, Deep learning through two-branch convolutional neural network for glaucoma diagnosis, in: Proceedings of the International Conference of Smart Health, 2017, pp. 191–201.
[18] K. Chatfield, K. Simonyan, A. Vedaldi, A. Zisserman, Return of the devil in the details: delving deep into convolutional nets, in: Proceedings of the British Machine Vision Conference, 2014.
[19] X. Chen, Y. Xu, D.W.K. Wong, T.Y. Wong, J. Liu, Glaucoma detection based on deep convolutional neural network, in: Proceedings of the Thirty-Seventh Annual International Conference on the IEEE Engineering in Medicine and Biology Society, Milan, Italy, 2015.
[20] X. Chen, Y. Xu, S. Yan, D.W.K. Wong, T.Y. Wong, J. Liu, Automatic feature learning for glaucoma detection based on deep learning, in: International Conference on Medical Image Computing and Computer-Assisted Intervention, 2015, pp. 669–677.
[21] J. Cheng, J. Liu, Y. Xu, F. Yin, D.W.K. Wong, N.M. Tan, D. Tao, C.Y. Cheng, T. Aung, T.Y. Wong, Superpixel classification based optic disc and optic cup segmentation for glaucoma screening, IEEE Trans. Med. Imaging 32 (6) (2013) 1019–1032.
[22] D.C. Ciresan, U. Meier, L.M. Gambardella, J. Schmidhuber, Convolutional neural network committees for handwritten character classification, in: Proceedings of the IEEE International Conference on Document Analysis and Recognition, Beijing, China, 2011, pp. 1135–1139.
[23] T.M. Cover, P.E. Hart, Nearest neighbor pattern classification, IEEE Trans. Inf. Theory 13 (1) (1967) 21–27.
[24] T. Damms, F. Dannheim, Sensitivity and specificity of optic disc parameters in chronic glaucoma, Investig. Ophthalmol. Visual Sci. 34 (7) (1993) 2246–2250.
[25] K. Dragomiretskiy, D. Zosso, Variational mode decomposition, IEEE Trans. Signal Process. 62 (3) (2014) 531–544.
[26] A.W. Dreher, K. Reiter, R.N. Weinreb, Spatially resolved birefringence of the retinal nerve fiber layer assessed with a retinal laser ellipsometer, Appl. Opt. 31 (1992) 3730–3735.
[27] S. Dua, U.R. Acharya, P. Chowriappa, V.S. Sree, Wavelet-based energy features for glaucomatous image classification, IEEE Trans. Inf. Technol. Biomed. 16 (1) (2012) 80–87.
[28] R.O. Duda, P.E. Hart, D.G. Stork, Pattern Classification, second edition, John Wiley and Sons, New York, 2001.
[29] J.P. Egan, Signal detection theory and ROC analysis, Series in Cognition and Perceptron Academic Press, New York Academic Press, New York, 1975.
[30] B. Fröba, A. Ernst, Face detection with the modified census transform, in: Proceedings of the Sixth International Conference on Automatic Face and Gesture Recognition, Seoul, South Korea, 2004, pp. 91–96.
[31] J.A. de la Fuente-Arriaga, E.M. Felipe-Riverón, E. Garduño-Calderón, Application of vascular bundle displacement in the optic disc for glaucoma detection using fundus images, Comput. Biol. Med. 47 (2014) 27–35.
[32] D. Gabor, Theory of communication, Part 1, J. Inst. Electr. Eng. 93 (1946) 429–441.
[33] M.M. Galloway, Texture classification using gray level run length, Comput. Graph. Image Proces. 4 (2) (1975) 172–179.
[34] J. Gillies, Empirical wavelet transform, IEEE Trans. Signal Process. 61 (2013) 3999–4002.
[35] Glaucoma Research Foundation, Five common glaucoma tests, 2017. Retrieved from https://www.glaucoma.org/glaucoma/diagnostic-tests.php.
[36] V. Gulshan, L. Peng, M. Coram, et al., Development and validation of a deep learning algorithm for detection of diabetic retinopathy in retinal fundus photographs, J. Am. Med. Assoc. 316 (22) (2016) 2402–2410.
[37] Y. Guo, G. Zhao, M. Pietikäinen, Texture classification using a linear configuration model based descriptor, in: Proceedings of the British Machine Vision Conference, 2011.
[38] M. Haddrill, C. Slonim, What causes glaucoma?, 2016. Retrieved from All About Vision http://www.allaboutvision.com/conditions/glaucoma-2-cause.htm.
[39] R.M. Haralick, K. Shnmugam, I. Dinstein, Textural features for image classification, IEE Trans. Syst. Man Cybern. 3 (6) (1973) 610–621.
[40] Y. Hayashi, T. Nakagawa, Y. Hatanaka, A. Aoyama, M. Kakogawa, T. Hara, H. Fujita, T. Yamamoto, Detection of retinal nerve fiber layer defects in retinal fundus images using Gabor filtering, Soc. Photo Opt. Instrum. Eng. 6514 (2007) 65142Z 8 pages.
[41] S. Hochreiter, J. Schmidhuber, Long short-term memory, Neural Comput. 9 (1997) 1735–1780.
[42] M. Hossein, J. Bonyandi, High myopic peripapillary atrophy; spectral domain optical coherence tomography features, J. Ophthalmic Vis. Res. 11 (1) (2016) 124–125.
[43] D. Huang, E.A. Swanson, C.P. Lin, J.S. Schuman, W.G. Stinson, W. Chang, M.R. Hee, T. Flotte, K. Gregory, C.A. Puliafito, J.G. Fujimoto, Optical coherence tomography, Science 254 (1991) 1778–1781.
[44] A. Hyvarinen, J. Karhunen, E. Oja, Independent Component Analysis, John Wiley & Sons, 2004.
[45] A. Issac, M.P. Sarathi, M.K. Dutta, An adaptive threshold based image processing technique for improved glaucoma detection and classification, Comput. Methods Progr. Biomed. 122 (2015) 229–244.
[46] G.D. Joshi, J. Sivaswamy, S.R. Krishnadas, Optic disc and cup segmentation from monocular color retinal images for glaucoma assessment, IEEE Trans. Med. Imaging 30 (6) (2011) 1192–1205.
[47] F. Jurie, B. Triggs, Creating efficient codebooks for visual recognition, in: Proceedings of the Tenth IEEE International Conference on Computer Vision, Los, Angeles, 2005.
[48] T.R. Kausu, V.P. Gopi, K.A. Wahid, W. Doma, S.I. Niwas, Combination of clinical and multiresolution features for glaucoma detection and its classification using fundus images, Biocybern. Biomed. Eng. (2018), doi:10.1016/j.bbe.2018.02.003.
[49] S.S. Keerthi, S.K. Shevade, C. Bhattacharyya, K.R.K. Murthy, Improvements to Platt's SMO algorithm for SVM classifier design, Neural Comput. 13 (3) (2001) 637–649.
[50] J.E.W. Koh, U.R. Acharya, Y. Hagiwara, U. Raghavendra, J.H. Tan, S.V. Sree, S.V. Bhandary, A.K. Rao, S. Sivaprasad, K.C. Chua, A. Laude, L. Tong, Diagnosis of retinal health in digital fundus images using continuous wavelet transform (CWT) and entropies, Comput. Biol. Med. 84 (2017) 89–97.
[51] J.E.W. Koh, E.Y.K. Ng, S.V. Bhandary, Y. Hagiwara, A. Laude, U.R. Acharya, Automated retinal health diagnosis using pyramid histogram of visual words and fisher vector techniques, Comput. Biol. Med. 92 (2018) 204–209.
[52] J.E.W. Koh, E.Y.K. Ng, S.V. Bhandary, A. Laude, U.R. Acharya, Automated detection of retinal health using PHOG and SURF features extracted from fundus images, in: Applied Intelligence, Springer, US, 2017, pp. 1–15.
[53] R. Kolar, Jan J, Detection of glaucomatous eye via color fundus images using fractal dimensions, Radio Eng. 17 (3) (2008) 109–114.
[54] A. Krizhevsky, I. Sutskever, G.E. Hinton, ImageNet classification with deep convolutional neural networks, Adv. Neural Inf. Proces. Syst. 12 (2012) 1097–1105.
[55] Y. LeCun, Y. Bengio, G. Hinton, Deep learning, Nature 521 (2015) 436–444.
[56] J.G. Lee, S. Jun, Y.W. Cho, H. Lee, G.B. Kim, J.B. Seo, N. Kim, Deep learning in medical imaging: general overview, Korean J. Radiol. 18 (4) (2017) 570–584.
[57] T.C. Lim, S. Chattopadhyay, U.R. Acharya, A survey and comparative study on the instruments for glaucoma, Med. Eng. Phys. 34 (2) (2012) 129–139.
[58] Y.Z. Lin, Z.H. Nie, H.W. Ma, Structural damage detection with automatic feature-extraction through deep learning, Comput. Aided Civ. Infrastruct. Eng. 32 (2017) 1025–1046.
[59] S. Maheshwari, R.B. Pachori, U.R. Acharya, Automated diagnosis of glaucoma using empirical wavelet transform and correntropy features extracted from fundus images, IEEE J. Biomed. Health Inf. 21 (3) (2017) 803–813.
[60] S. Maheshwari, R.B. Pachori, V. Kanhangad, S.V. Bhandary, U.R. Acharya, Iterative variational mode decomposition based automated detection of glaucoma using fundus images, Comput. Biol. Med. 88 (2017) 142–149.
[61] S. Mallat, A theory for multi-resolution signal decomposition: the wavelet representation", IEEE Trans. Pattern Anal. Mach. Intell. 11 (7) (1989) 674–693.
[62] B.B. Mandelbrot, Geometry of Nature, Freeman, San Francisco, 1983.
[63] J. Marsden, Glaucoma: the "silent thief of sight, in: Nursing Times, 110, 2014, pp. 20–22. https://www.nursingtimes.net/roles/older-people-nurses/glaucoma-the-silent-thief-of-sight/5075669.article
[64] Medical Image Analysis Group, MIAG, 2015. Retrieved from http://medimrg.webs.ull.es/.
[65] M.B. Merickel, M.D. Abràmoff, M. Sonka, X. Wu, Segmentation of the optic nerve head combining pixel classification and graph search, Soc. Photo Opt. Instrum. Eng. 6512 (2007), doi:10.1117/12.710588.
[66] P.S. Mittapalli, G.B. Kande, Segmentation of optic disc and optic cup from digital fundus images for the assessment of glaucoma, Biomed. Signal Process. Control 24 (2016) 34–46.
[67] M.R.K. Mookiah, U.R. Acharya, K.C. Chua, C.M. Lim, E.Y.K. Ng, M.M. Mushrif, A. Laude, Automated detection of optic disc in retinal fundus images using intuitionistic fuzzy histon segmentation, Proc. Inst. Mech. Eng. Part H J. Eng. Med. 227 (1) (2013) 37–49.
[68] M.R.K. Mookiah, U.R. Acharya, C.M. Lim, A. Petznick, J.S. Suri, Data mining technique for automated diagnosis of glaucoma using higher order spectra and wavelet energy features, Knowl. Based Syst. 33 (2012) 73–82.
[69] C. Muramatsu, Y. Hatanaka, A. Sawada, T. Yamamoto, H. Fujita, Computerized detection of peripapillary chorioretinal atrophy by texture analysis, in: Proceedings of the Third Annual International Conference of the IEEE Engineering in Medicine and Biology Society, Boston, MA USA, 2011.
[70] C. Muramatsu, Y. Hayashi, A. Sawada, Y. Hatanaka, T. Hara, T. Yamamoto, H. Fujita, Detection of retinal nerve fiber layer defects on retinal fundus images for early diagnosis of glaucoma, J. Biomed. Opt. 15 (1) (2010) 016021, doi:10.1117/1.3322388.
[71] J. Nayak, U.R. Acharya, P.S. Bhat, N. Shetty, T.C. Lim, Automated diagnosis of glaucoma using digital fundus images, J. Med. Syst. 33 (5) (2009) 337–346.
[72] M. Ng, P.A. Sample, J.P. Pascual, L.M. Zangwill, C.A. Girkin, J.M. Liebmann, R.N. Weinreb, L. Racette, Comparison of visual field severity classification systems for glaucoma, J. Glaucoma 21 (8) (2012) 551–561.
[73] C.L. Nikias, A.P. Petropulu, Higher-Order Spectra Analysis: A Nonlinear Signal Processing Framework, PTR Prentice Hall, Englewood Cliffs, NJ, 1993.
[74] K.P. Noronha, U.R. Acharya, K.P. Nayak, R.J. Martis, S.V. Bhandary, Automated classification of glaucoma stages using higher order cumulant features, Biomed. Signal Process. Control 10 (2014) 174–183.
[75] J. Odstrcilik, R. Kolar, R.P. Tornow, J. Jan, A. Budai, M. Mayer, M. Vodakova, R. Larmmer, M. Lamos, Z. Kuna, J. Gazarek, T. Kubena, P. Cernosek,

M. Ronzhina, Thickness related textural properties of retinal nerve fiber layer in color fundus images, Comput. Med. Imaging Graph. 38 (6) (2014) 508–516.
[76] J.E. Oh, H.K. Yang, W.G. Kim, J.M. Huang, Automatic computer-aided diagnosis of retinal nerve fiber layer defects using fundus photographs in optic neuropathy, Investig. Ophthalmol. Visual Sci. 56 (6) (2015) 2872–2879.
[77] J.I. Orlando, E. Prokofyeva, M. del Fresno, M.B. Blaschko, Convolutional neural network transfer for automated glaucoma identification, in: Proceedings of the Twelfth International Symposium on Medical Information Processing and Analysis, Tandil, Argentina, 2017 10160.
[78] Y. Ou, Glaucoma and the importance of the eye's drainage system, 2017. Retrieved from the BrightFocus Foundation https://www.brightfocus.org/glaucoma/article/glaucoma-and-importance-eyes-drainage-system.
[79] K. Pearson, On lines and planes of closest fit to systems of points in space, Philos. Mag. 2 (11) (1901) 559–572.
[80] S.M. Pizer, E.P. Amburn, J.D. Austin, R. Cromarrtie, A. Geselowitz, T. Greer, B.terHaar Romeny, J.B. Zimmerman, K. Zuiderveld, Adaptive histogram equalization and its variations, Comput.Vis. Graph. Image Process. 39 (3) (1987) 355–368.
[81] H.A. Quigley, W.R. Green, The histology of human glaucoma cupping and optic nerve damage: clinical correlation in 21 eyes, Ophthalmology 86 (10) (1979) 1803–1830.
[82] J. Radon, On the determination of functions from their integral values along certain manifolds, IEEE Trans. Med. Imaging 5 (1986) 170–176.
[83] U. Raghavendra, S.V. Bhandary, A. Gudigar, U.R. Acharya, Novel expert system for glaucoma identification using non-parametric spatial envelope energy spectrum with fundus images, Biocybern. Biomed. Eng. (2017), doi:10.1016/j.bbe.2017.11.002.
[84] U. Raghavendra, H. Fujita, S.V. Bhandary, A. Gudigar, J.H. Tan, U.R. Acharya, Deep convolutional neural network for accurate diagnosis of glaucoma using digital fundus images, Inf. Sci. 441 (2018) 41–49.
[85] R.P. Rajaiah, R.J. Britto, Optic disc boundary detection and cup segmentation for prediction of glaucoma, Int. J. Sci. Eng. Technol. Res. 3 (10) (2014) 2665–2672.
[86] P. Sermanet, D. Eigen, X. Zhang, M. Mathieu, R. Fergus, Y. LeCun, OverFeat: integrated recognition, localization and detection using convolutional networks, in: Proceedings of the International Conference on Learning Representation, 2014.
[87] A. Shaikh, J.F. Salmon, The role of scanning laser polarimetry using the GDx variable corneal compensator in the management of glaucoma suspects, Br. J. Ophthalmol. 90 (2006) 1454–1457.
[88] C.E. Shannon, A mathematical theory of communication, Bell Syst. Tech. J. 27 (1948) 376–656.
[89] P. Sharma, P.A. Sample, L.M. Zangwill, J.S. Schuman, Diagnostic tools for glaucoma detection and management, Surv. Ophthalmol. 53 (6) (2008) S17–S32.
[90] G.A. Siam, M.E. Gheith, D.S. de Barros, A.P. Lin, M.R. Moster, Limitations of the Heidelberg retina tomograph, Ophthalmic Surg. Lasers Imaging Off. J. Int. Soc. Imaging Eye 39 (3) (2008) 262–264.
[91] A. Singh, M.K. Dutta, M.P. Sarathi, V. Uher, R. Burget, Image processing based automatic diagnosis of glaucoma using wavelet features for segmented optic disc from fundus image, Comput. Methods Progr. Biomed. 124 (2016) 108–120.
[92] M. Singh, M. Singh, J. Virk, Glaucoma detection techniques: a review, Int. J. Comput. Sci. Commun. 6 (2) (2015) 66–76.
[93] F. Song, D. Mei, H. Li, Feature selection based on linear discriminant analysis, in: Proceedings of the International Conference on Intelligence System Design and Engineering Application, Changsha, China, 2010.
[94] Student, The probable error of a mean, Biometrika 6 (1) (1908) 1–25.
[95] V.K. Sudarshan, U.R. Acharya, E.Y.K. Ng, R.S. Tan, S.M. Chou, D.N. Ghista, An integrated index for automated detection of infarcted myocardium from cross–sectional echocardiograms using texton-based features (Part 1), Comput. Biol. Med. 71 (2016) 231–240.
[96] N. Thakur, M. Juneja, Survey on segmentation and classification approaches of optic cup and optic disc for diagnosis of glaucoma, Biomed. Signal Process. Control 42 (2018) 162–189.
[97] Y.C. Tham, X. Li, T.Y. Wong, H.A. Quigley, T. Aung, C.Y. Cheng, Global prevalence of glaucoma and projections of glaucoma burden through 2040: a systematic review and meta-analysis, Ophthalmology 121 (11) (2014) 2081–2091.
[98] R. Thomas, K. Loibl, R.S. Parikh, Evaluation of a glaucoma patient, Indian J. Ophthalmol. 59 (2011) S43–S52.
[99] D.S.W. Ting, C.Y.L. Cheung, G. Lim, G.S.W. Tan, N.D. Quang, A. Gan, H. Hamzah, R. Garcia-Franco, I.Y.S. Yeo, S.Y. Lee, E.Y.M. Wong, C. Sabanayagarn, M. Baskaran, F. Ibrahim, N.C. Tan, E.A. Finkelstein, E.L. Lamoureux, I.Y. Wong, N.M. Bressler, S. Sivaprasad, R. Varma, J.B. Jonas, M.G. He, C.Y. Cheng, G.C.M. Cheung, T. Aung, W. Hsu, M.L. Lee, T.Y. Wong, Development and validation of a deep learning system for diabetic retinopathy and related eye diseases using retinal images from multiethnic populations with diabetes, J. Am. Med. Assoc. 318 (22) (2017) 2212–2223.
[100] V. Vapnik, I. Guyon, T. Hastie, Support vector machines, Mach. Learn. 20 (1995) 273–297.
[101] R. Varma, P.P. Lee, I. Goldberg, S. Kotak, An assessment of the health and economic burdens of glaucoma, Am. J. Ophthalmol. 152 (4) (2011) 515–522.
[102] R.H. Webb, G.W. Hughes, F.C. Delori, Confocal scanning laser ophthalmoscope, Appl. Opt. 26 (8) (1987) 1492–1499.
[103] F. Wilcoxon, Individuals comparisons by ranking methods, Biom. Bull. 1 (6) (1945) 80–83.
[104] Y. Xu, S. Lin, D.W.K. Wong, J. Liu, D. Xu, Efficient reconstruction-based optic cup localization for glaucoma screening, in: Proceedings of the International Conference on Medical Image Computing and Computer-Assisted Intervention, 2013, pp. 445–452.
[105] S. Yan, D. Xu, B. Zhang, H.J. Zhang, Q. Yang, S. Lin, Graph embedding and extensions: a general framework for dimensionality reduction, IEEE Trans. Pattern Anal. Mach. Intell. 29 (1) (2006) 40–51.
[106] B. Yegnanarayana, Artificial Neural Networks, Prentice-Hall of India, New Delhi, 1999.
[107] Z. Zhang, R. Srivastava, H. Liu, X. Chen, L. Duan, D.W.K. Wong, C.K. Kwoh, T.Y. Wong, J. Liu, A survey on computer-aided diagnosis for ocular diseases, BMC Med. Inf. Decis. Mak. 14 (80) (2014) 1–29.
[108] J. Zilly, J.M. Buhmann, D. Mahapatra, Glaucoma detection using entropy sampling and ensemble learning for automatic optic cup and disc segmentation, Comput. Med. Imaging Graph. 55 (2017) 28–41.